



Howell, L., Brown, C. S. and Egan, S. S. (2021) Deep geothermal energy in northern England: Insights from 3D finite difference temperature modelling. *Computers and Geosciences*, 147, 104661.  
(doi: [10.1016/j.cageo.2020.104661](https://doi.org/10.1016/j.cageo.2020.104661))

There may be differences between this version and the published version. You are advised to consult the publisher's version if you wish to cite from it.

<http://eprints.gla.ac.uk/259766/>

Deposited on 1 December 2021

Enlighten – Research publications by members of the University of Glasgow  
<http://eprints.gla.ac.uk>

# 1 Deep geothermal energy in northern 2 England: insights from 3D finite difference 3 temperature modelling

4 Louis Howell<sup>1\*</sup>, Christopher S. Brown<sup>2</sup>, Stuart S. Egan<sup>1</sup>

## 5 Authorship statement

- 6 • Louis Howell: compiled metadata, constructed model, wrote manuscript
- 7 • Christopher Brown: helped construct model and write manuscript
- 8 • Stuart Egan: helped construct model and write manuscript

## 9 Code availability

10 Matlab-based source code is freely available via [https://github.com/lphowell/Geothermal-](https://github.com/lphowell/Geothermal-Modelling/tree/master/Geothermal_NEngland)  
11 [Modelling/tree/master/Geothermal\\_NEngland](https://github.com/lphowell/Geothermal-Modelling/tree/master/Geothermal_NEngland) or by contacting the lead author.

## 12 Highlights

- 13 • Subsurface temperature and heat flow maps for northern England are produced by  
14 temperature modelling
- 15 • These maps are more resolute and geologically more realistic relative to equivalent  
16 contoured maps for the UK
- 17 • Temperature models highlight ‘hot spots’ associated with granite intrusions and geological  
18 structure
- 19 • This technique comprises a useful tool for deep geothermal energy exploration

## 20 Key words

21 Geothermal Energy; Temperature; Finite Difference; Numerical Modelling

## 22 Abstract

23 Many of the most widely used deep geothermal resource maps for the UK are produced by  
24 contouring around sparsely distributed and often unreliable data points. We thus present a  
25 MATLAB-based 3D finite difference temperature modelling methodology, which provides a means  
26 for producing more resolute and geologically realistic versions of these maps. Our case study area in  
27 northern England represents an area where both sedimentary basins and radiothermal granite  
28 bodies comprise potential geothermal resources. We divide our 3D model into geological units,  
29 which are then assigned separate thermal properties. Assuming conductive heat transfer and  
30 steady-state and fixed boundary conditions, we calculate 3D regional subsurface temperature. Due  
31 to our averaging technique for thermal properties, the resolution of our geological model is scarcely  
32 compromised with respect to similar finite element methods. One predicted ‘hot spot’ at 1 km depth  
33 in the central part of our case study area corresponds with the granitic North Pennine Batholith.  
34 Other shallow hot spots correspond with thermally insulating sedimentary rock units and geological  
35 structures that incorporate these units. Predictive heat flow density maps highlight areas with  
36 accelerated surface heat flow associated with shallow conductive basement rock and heat producing  
37 granite bodies. Our predicted subsurface temperatures show broad similarities with measured

38 equilibrium borehole temperatures. Inaccuracies may relate to convective heat transfer involving  
39 fault systems, or input variables relating to the geological model. Our predictive subsurface  
40 temperature and heat flow density maps are more resolute and geologically realistic relative to pre-  
41 existing contoured maps. The method presented here represents a useful tool for understanding  
42 controls on subsurface temperature distribution and geothermal potential.

## 43 1. Introduction

44 Geothermal may provide one alternative energy resource as part of a worldwide effort to  
45 reduce our reliance on fossil fuels and combat climate change (Zhang *et al.*, 2019). Nonetheless, the  
46 UK lags behind its neighboring north-western European counterparts with regards to harnessing its  
47 deep geothermal potential. This is reflected by the fewer number of geothermal boreholes drilled  
48 (Gluyas *et al.*, 2018), the smaller contribution of geothermal towards the combined energy mix (BP  
49 Energy Outlook, 2019), smaller research output, and the now somewhat outdated subsurface  
50 temperature and heat flow maps for the UK (e.g. Downing and Gray, 1986a, 1986b; Lee *et al.*, 1987;  
51 Busby, 2010, 2014; Busby *et al.* 2011). These maps are commonly constructed by contouring around  
52 sparsely distributed and sometimes unreliable data points (Rollin, 1995), rendering them often  
53 irresolute and inaccurate (Fig. 1). Despite increasing interest in UK geothermal, as several recent and  
54 ongoing projects testify to (Younger *et al.*, 2016; Adams *et al.*, 2019; Monaghan *et al.*, 2019; Paulillo  
55 *et al.*, 2020), the reliance on these quasi-resource maps remains a cause for concern.

56 Where data is either sparse or unreliable, predictive modelling may comprise a useful tool  
57 (Pérez-Zárte *et al.*, 2019). Numerically based 3D regional subsurface temperature models help  
58 communicate regional geothermal potential (e.g. Cacace *et al.*, 2010; Calcagno *et al.*, 2014; Fuchs  
59 and Balling, 2016). Such models typically implement elaborate, but often complex and,  
60 consequently, less reproducible finite element techniques (e.g. Cacace and Jacquy, 2017). Finite  
61 difference analyses offer less computationally intensive alternatives to these methods. Although the  
62 resolution and accuracy of finite difference models are limited by the typically rectangular nodal  
63 arrangements of finite difference grids, for smaller problems, such as for the (<1 km) area around a  
64 geothermal well head, a finite difference grid can be sufficiently scaled to compromise between  
65 both model accuracy and rapid model convergence (e.g. Croucher *et al.*, 2020; Keller *et al.*, 2020).  
66 Finite difference techniques are also adopted for subsurface temperature problems where the  
67 geological uncertainty is greater than the model resolution, such as for the deep lithosphere and  
68 mantle (e.g. Fullea *et al.*, 2009). However, for intermediate scale problems, such as for subsurface  
69 temperature and heat flow density mapping (e.g. Fig. 1), a combination of the often inflexible finite  
70 difference temperature grids, and the coarse model resolutions required to reduce run times, can  
71 render such methods too inaccurate (*cf.* Gibson *et al.*, 2008).

72 We present an innovative 3D finite difference thermal modelling method that is used to  
73 predict deep subsurface temperature and heat flow density in northern England. Due to our  
74 averaging techniques for thermal conductivity and radiogenic heat production values, the resolution  
75 of our geological model is effectively far greater than the temperature model's coarse nodal spacing.  
76 Consequently, the accuracy of our model is not compromised to reduce computational intensity. We  
77 document formulae and include MATLAB script with supplementary information for 3D steady-state  
78 conductive heat transfer. Comparisons are made between results from our simulations and  
79 measured borehole temperatures and heat flow densities. This technique represents some key  
80 influences of complex geological structure on subsurface temperature distribution. Its main  
81 strengths are its robustness, simplicity and reproducibility relative to more elaborate finite element  
82 techniques. Compared to other finite difference techniques, our methodology offers more resolute

83 and geologically more realistic solutions. We present and discuss the UK's first deep 3D temperature  
84 model and associated geothermal resource maps.

## 85 2. Study area: northern England

86 Our case study comprises an area of the UK where both sedimentary basins and ancient  
87 granite bodies contribute to potential geothermal resources (Gluyas *et al.*, 2018). Together, it  
88 comprises the northern part of the Lake District, the north-east of England and the Scottish borders  
89 (Fig. 2). The primary energy demand for this region is roughly along the north-east coast and  
90 includes Newcastle-upon-Tyne and Sunderland. Besides Carlisle, the remainder of our study area is  
91 amongst the most sparsely populated areas of England. Ideally for the purposes of our study, this is  
92 an area that has had widely documented but ultimately unsuccessful in geothermal exploration  
93 (Gluyas *et al.*, 2018).

94 Despite the magnitude of recent investments in geothermal exploration in northern England  
95 (Manning *et al.*, 2007; Hirst, 2012; Younger *et al.*, 2016), what we know about deep subsurface  
96 temperatures and heat flow in the region is based upon somewhat outdated quasi-resource maps  
97 (e.g. Downing and Gray, 1986a) (Fig. 1). In our study area, for example, maps depicting temperature  
98 at 1 km depth are based on contours around just six temperature data points (Fig. 3). These data are  
99 situated predominantly within the Carboniferous basins of the region and only two of these are  
100 equilibrium measurements (Burley *et al.*, 1984). On further inspection of these maps and the UK  
101 Geothermal Catalogue (Burley *et al.*, 1984), heat flow density maps for this region are based on  
102 contours around just 9 data points (Fig. 1b). Based on the type of conductivity and temperature  
103 measurement, amongst other factors, Rollin (1995) graded the reliability of these data with quality  
104 functions from 0 to 1, with 1 being good and 0 being poor. The highest grade awarded for a data  
105 point in our study area was 0.65. Just five data points surpassed 0.25.

## 106 3. Data

107 A series of surface elevation grids comprise the primary dataset of our study (Fig. 4). A  
108 structural model of the Carboniferous-Permian basins of our study area is based on the seismic  
109 interpretations of Chadwick *et al.* (1995) (*cf.* Terrington and Thorpe, 2013). The structure of pre-  
110 Carboniferous basement bound Caledonian granites are based upon the gravity interpretations of  
111 Kimbell *et al.* (2010). The bases of these granite intrusions are assumed flat at 9 km depth (*cf.*  
112 Kimbell *et al.*, 2010) (Fig. 4). Our geological model does not include the Cheviot granites or other  
113 granites along the Southern Uplands, which are located beyond the northern margin of our study  
114 area. Likewise, our geological model neglects all fault zones within our study area. Our surface  
115 elevation grids are extrapolated to fill a 110 km by 150 km volume. The coordinates at which  
116 elevation values are given each correspond to separate nodes within our temperature grid and are  
117 uniformly spaced at 500 m.

118 Surface elevation grids separate geological units that are assigned distinct thermal  
119 properties within our temperature model (Table 1). Thermal conductivity of the crust is a function of  
120 temperature and pressure, as well as composition (Norden *et al.*, 2020); therefore, conductivity of  
121 the middle to lower crust decreases linearly with depth, from  $3.1 \text{ W m}^{-1} \text{ K}^{-1}$  at 9 km depth, to  $2.2 \text{ W}$   
122  $\text{m}^{-1} \text{ K}^{-1}$  at 30 km depth (*cf.* Vilá *et al.*, 2010). Thermal properties for basement rock and basin fill are  
123 based on numerous literary sources (Table 1). Borehole temperatures for comparison with our  
124 modelled subsurface temperature grid are derived from the UK Geothermal Catalogue (Burley *et al.*,  
125 1984) and published literature (e.g. Younger *et al.*, 2016). Typically, finite difference techniques  
126 dictate that the thermal property matrices within temperature models are divided into a series of

127 variably sized cuboids, the volume of which are defined by the nodal spacing of the temperature grid  
128 (e.g. Fullea *et al.*, 2009). However, in Section 4.3 we detail how more geologically realistic thermal  
129 property matrices may be derived from a geological model, whilst still implementing a less  
130 computationally intensive finite difference methodology and coarse nodal spacing.

## 131 4. Methods

132 A summary of our modelling approach is illustrated in Figure 5. These methods may be  
133 amended depending on the characteristics of geological models or the specifications of subsurface  
134 temperature models, although the crux of this technique may remain unchanged. We recommend  
135 that the meshing process is treated separately from temperature simulation, to reduce memory  
136 drainage and ultimately reduce temperature convergence times.

### 137 4.1 Governing equations

138 To calculate subsurface temperature, we solve a steady-state conductive heat equation, or  
139 diffusion equation according to Fourier's law. The diffusion equation operates on the basis of energy  
140 conservation and relates heat flow ( $q$ ) to temperature gradients ( $\nabla T$ ). In its differential form, it can  
141 be given as:

$$q = -k \nabla T$$

142 (Eq. 1)

143 where  $k$  is the bulk rock thermal conductivity tensor. Temperature change experienced by each  
144 node within the temperature grid is equal to the heat conducted into or out of a node, plus  
145 radiogenic heat production ( $Q$ ). Thus, the following relationship between change in heat flow ( $\nabla q$ )  
146 and time ( $t$ ) can be determined:

$$(\rho c) \frac{\partial T}{\partial t} = -\nabla q + Q$$

147 (Eq. 2)

148 where  $\rho$  is the bulk rock density and  $c$  is the bulk specific heat capacity. When Equation 1 is  
149 substituted into Equation 2, the equation for transient diffusion is given:

$$(\rho c) \frac{\partial T}{\partial t} = \nabla(k \nabla T) + Q$$

150 (Eq. 3)

151 Under steady-state conditions, any transient effect is neglected. Therefore, the equation can be  
152 rearranged further as thus:

$$\nabla(k \nabla T) = -Q$$

153 (Eq. 4)

154 This equation is solved for the temperature using a 3D implementation of the finite difference  
155 methodology with algorithms developed using the MATLAB (Mathworks) numerical computing  
156 environment.

### 157 4.2 Boundary conditions and model validation

158 The solution to Equation 4 using the finite difference method requires definition of  
159 boundary conditions. For subsurface thermal modelling, we adopt an upper boundary (surface)

160 temperature of 10 °C, in concurrence with UK annual mean average air temperature (Busby *et al.*,  
161 2009). The lower boundary temperature at the base of our model represents a more irreconcilable  
162 problem. The base of the lithosphere is at a depth of approximately 125 km beneath much of north-  
163 western Europe and is represented by the 1333 °C isotherm (Sclater and Christie, 1980).

164 To validate the differential solution against an analytical solution in one-dimension and  
165 determine the likely lithosphere-scale geothermal structure of our case study area, we reiterate the  
166 linear equation until an asymptotic solution, our modelled geothermal gradient, is reached (Fig. 6).  
167 When adopting a uniform grid spacing of 1 km, the modelled geothermal gradient approaches its  
168 steady state solution after approximately 10,000 iterations. To reduce convergence time, the  
169 temperature matrix can be populated with a pre-defined temperature distribution (e.g. Bayer *et al.*,  
170 1997) or be thermally conditioned using temperatures from previous model simulations. Besides  
171 boundary temperatures, thermal conductivity has a primary control on the geothermal gradient. The  
172 decreased geothermal gradient with depth, after 30 km, reflects the increased thermal conductivity  
173 of mantle rock relative to crustal rock below the Moho boundary (e.g. Čermác and Rybach, 1982)  
174 (Table 1). With the addition of radiogenic heat production, the modelled geothermal gradient forms  
175 a convex upwards curve.

176 The lateral boundaries of our 3D model, in the  $x$  and  $y$  directions, are closed. Thus  $\delta T/\delta x =$   
177  $0$ , and  $\delta T/\delta y = 0$ . This implies no heat is transferred beyond the lateral boundaries of the model and  
178 that these boundaries represent surfaces of symmetry. Neither of these assumptions fit reality but  
179 they provide approximations for complex geological structures. To reduce the potentially  
180 detrimental effects of these boundaries, a wide aspect model ratio is necessary. Increasing the  
181 dimensions of the temperature model to three decreases convergence time by the nodal widths of  
182 the model in both the  $x$  and  $y$  directions, by 150 km and 110 km respectively for our model of  
183 northern England. To reduce computational intensity, therefore, we adopt a shallow lower boundary  
184 condition of 665.6 °C at 30 km depth, in concurrence with results from our one-dimensional  
185 lithosphere-scale model (Fig. 6), and assume the resolution of our model in terms of node spacing  
186 within the temperature grid is 500 m.

#### 187 4.3 Approximation of geological model

188 The shortcomings of a finite difference model relate to its inflexibility. In implementing a  
189 finite difference methodology, the value for radiogenic heat production of a single node comprises  
190 heat production for the entire cubic rock volume for which that node represents. Likewise, for  
191 thermal conductivity, one value calculated between two adjacent nodes represents the combined  
192 conductivity for that transect of rock, which is 500 m long in this instance. Where the modelled rock  
193 volume is structurally complex or characteristically heterogeneous, therefore, thermal properties for  
194 individual temperature nodes may be misrepresentative, rendering the temperature model  
195 inaccurate. These issues are exacerbated when coarse model resolutions are necessary, as they are  
196 here. We thus demonstrate how more representative 3D thermal property matrices may be derived  
197 from structurally complex geological models.

198 Thermal properties for distinct points within the bounds of our 3D temperature model  
199 reflect the corresponding depths of those points at specific  $x$  and  $y$  coordinates relative to the  
200 depths of geological boundaries in a geological model. Depending on the preassigned distance  
201 between temperature nodes ( $\nabla i$ ), the corresponding depth of a temperature node in a geological  
202 model is determined by:

$$depth = (z - 1) \nabla i$$

203 (Eq. 5)

204 Where  $z$  is a reference to the depth corresponding to the position of a given node within the  
205 temperature matrix.

206 Geological boundaries separate the numerous units of our geological model, which are assigned a  
207 series of distinct thermal properties (Table 1). So that we may avoid removing any of our geological  
208 model that is situated above sea level, the depths of geological horizons are given relative to surface  
209 elevation.

#### 210 4.3.1 Thermal conductivity matrices

211 We overcome resolution issues for thermal conductivity tensors between adjacent  
212 temperature nodes, i.e.  $k_{i+1/2}$  and  $k_{i-1/2}$ , by finding the harmonic mean (Hantschel and Kauerauf,  
213 2009) of multiple thermal conductivity values at uniformly spaced points between the respective  
214 nodes. Depending on the interval spacing resolution ( $res$ ) of sampled  $k$  points relative to  
215 temperature node spacing ( $\nabla i$ ), the distance between these sampling points ( $ss$ ) is determined as:

$$ss = \nabla i / res$$

216 (Eq. 6)

217 We adopt a resolution 50 times that of our temperature node spacing so that  $ss = 10$  m.

218 For each node within our temperature matrix there are references to depths of geological  
219 boundaries at corresponding  $x$  and  $y$  coordinates of our geological model. The precision of these  
220 depth values is not fixed to the resolution of our temperature model. Therefore, determining  
221 thermal conductivity values for distinct points at  $x$  and  $y$  coordinates between vertically adjacent  
222 temperature nodes based on their corresponding depths within a geological model is  
223 uncomplicated. However, as inputted spatial data for geological boundaries are limited to the  $x$  and  
224  $y$  coordinates of our temperature matrix, we may not apply this exact method to determine more  
225 representative thermal conductivity tensors laterally in between temperature nodes. To avoid  
226 inputting finer and more computationally intensive spatial data for geological boundaries, we  
227 interpolate depths of geological boundaries between laterally adjacent temperature nodes. These  
228 interpolated depths are used as a basis for determining  $k$  values in between laterally adjacent  
229 temperature nodes. The harmonic mean of these values may then be determined.

#### 230 4.3.2 Radiogenic heat production matrices

231 Poor resolutions for  $Q$  value matrices are not as detrimental to the accuracy of predictive  
232 subsurface temperature models as  $k$  value matrices. Nonetheless, more representative matrices of  
233  $Q$  values may be attained by adopting similar approaches to those just described for thermal  
234 conductivity. We determine  $Q$  values for multiple points up to half the temperature node spacing  
235 away from a given temperature node in the  $x$ ,  $y$  and  $z$  directions, which is 250 m in this instance. We  
236 manage this by adopting the same technique for determining  $k$  values at points in between  
237 temperature nodes in the  $z$  direction, and the  $x$  and  $y$  directions respectively. The arithmetic mean  
238 of these values is then determined (Hantschel and Kauerauf, 2009).

239 Figure 7 illustrates the benefit of deriving more accurate thermal property matrices from  
240 geological models in this way. Compared with finding the harmonic mean between just two  
241 conductivity values at points corresponding to adjacent temperature nodes, our more accurate  
242 thermal conductivity matrix is smoother. Sharp lateral conductivity changes correspond only to  
243 steeply dipping beds or fault offsets in this more accurate scenario (Fig. 7a), rather than also

244 shallowly dipping beds or the variable dips of beds with vertical thicknesses less than our  
245 temperature node spacing (Fig. 7b).

## 246 5. 3D temperature simulation

247 Our 3D subsurface temperature model reflects the controls of geological structure on  
248 vertical and lateral heat transfer and heat production. Temperatures calculated at depths of less  
249 than approximately 5 km are influenced by a combination of sedimentary basin fill and heat  
250 producing granite intrusions within the basement. At depths greater than 5 km, the basement has a  
251 predominant control on temperature distribution. We ignore parts of our model that are less than  
252 10 km away from the lateral boundaries that are more strongly influenced by boundary conditions.

### 253 5.1 Predicted shallow subsurface temperatures

254 The dominant 'hot spots' at 1 km depth are situated upon the central part of the Alston  
255 Block (Fig. 2a), the northern part of the Solway Syncline, the southern part of the Bewcastle  
256 Anticline, along the Vale of Eden and along the eastern margins of the Alston Block, and the  
257 Stainmore Trough (Fig. 8a). The modelled hot spot at 1 km depth on the central part of the Alston  
258 Block, where temperatures reach 46 °C, correlates strongly with the North Pennine Batholith (Fig.  
259 2b). However, the absence of any such hot spot in the Lake District, which is underpinned by the  
260 Lake District Batholith, at 1 km depth suggests that other factors influence this particular hot spot.  
261 We suggest that elevated temperatures on the Alston Block are influenced also by the local, variably  
262 thick, and comparatively insulating Carboniferous cover (*cf.* Bott *et al.*, 1972) (Fig. 4). This cover  
263 thickens towards the east and incorporates progressively younger and more insulating coal-bearing  
264 strata. These trends may account for the preservation of greater heat at 1 km depth towards the  
265 vertically adjacent eastern margin of the heat producing North Pennine Batholith, despite the  
266 eastwards thinning of this structure here (Kimbell *et al.*, 2010).

267 Owing to the comparatively thick and thermally insulating sedimentary fill preserved in the  
268 Vale of Eden Basin and lateral heat transfer from the radiothermal Lake District and North Pennine  
269 batholiths, our 3D subsurface temperature model predicts elevated temperatures at 1 km in this  
270 region, up to 43 °C (Fig. 8a). The parallel, NNE-SSW orientated Solway Syncline and Bewcastle  
271 Anticline provide more interesting thermal anomalies at 1 km depth. The northern part of the  
272 Solway Syncline, is comparatively hot at 1 km depth, up to 43 °C. Towards the south where this  
273 structure plunges, modelled temperatures at 1 km decrease to less than 39 °C. Conversely, the  
274 northern part of the Bewcastle Anticline is coolest, less than 37 °C, where thermally conductive pre-  
275 Carboniferous basement rock is shallowest. Where this structure also plunges to the south and  
276 preserves progressively thicker and younger insulating Carboniferous strata, temperatures increase  
277 up to 43 °C. Some of these thermal trends may be explained by the non-uniform presence and  
278 comparative thicknesses of coal-bearing and thermally insulating strata in this part of the  
279 Northumberland-Solway Basin. Some other thermal trends, however, may instead be explained by  
280 the vertical distributions of variably conductive rock units within the subsurface and the effects of  
281 these distributions on geothermal gradients at different depths. Transitioning from relatively  
282 insulating to conducting rock units with depth results in a decreased geothermal gradient with  
283 depth. The opposite arrangement results in an increased geothermal gradient with depth. Because  
284 the thermally insulating Pennine Coal Measures Group is at depths greater than 2 km to the south of  
285 the Solway Syncline, towards where the fold plunges, the geothermal gradient at these depths here  
286 is greater. Resulting temperatures at shallower depths, 1 km depth, are less. In contrast, in the  
287 northern part of the Solway Syncline, the thermally insulating Coal Measures are at depths between

288 0.5 and 2 km. As a result, the geothermal gradient is steepest at these depths and temperatures at 1  
289 km are comparatively elevated.

## 290 5.2 Predicted deep subsurface temperatures

291 Maximum vertical sedimentary basin thickness in our study area is approximately 8 km.  
292 Around these depths, little is known about the characteristics of basin fill (*cf.* Chadwick *et al.*, 1995)  
293 so differentiating thermal properties is difficult. The two main hot spots for these depths are  
294 associated with the radiothermal Lake District and North Pennine batholiths, where temperatures  
295 reach up to 154 °C (Fig. 8c). Faintly elevated temperatures at 5 km depth (Fig. 8b) are associated  
296 with the Solway Syncline and the eastwards thickening of Carboniferous strata within the northern  
297 Pennine Basin. At 7 km depth, elevated temperatures associated with the Solway Syncline are  
298 diminished further, as the modelled geotherm equilibrates laterally as it approaches the lower  
299 boundary condition (Fig. 8c). Slight local temperature elevations may be associated with the greater  
300 thicknesses of Carboniferous strata towards the east of our study area, up to 190 °C. At these  
301 depths, however, any other sources of localized temperature anomalies are dwarfed by comparison  
302 with anomalies due to the Lake District and North Pennine batholiths.

## 303 5.3 Predicted isotherm depth

304 By cubically interpolating vertically between temperature nodes, we determine depth to the  
305 100 °C isotherm across our study area. Depth to this temperature boundary varies between  
306 approximately 2.87 km and 3.51 km below surface in our study area (Fig. 9). The modelled isotherm  
307 is shallowest in the Lake District, although boundary conditions may exaggerate these shallow  
308 depths. The isotherm is also shallower than 3 km in the Alston Block, in the centre of our study area  
309 and towards Newcastle-upon-Tyne, suggesting that the two radiothermal granite intrusions of our  
310 study area strongly influence these depths. Markedly shallower depths, between approximately 3  
311 km and 3.2 km below surface, for the isotherm are also predicted for the Solway Basin, the Vale of  
312 Eden Basin and the eastern part of our study area. In these areas, comparatively thick Pennine Coal  
313 Measures Group successions are preserved. The greatest depths to the 100 °C isotherm are  
314 predicted in the western and central parts of the Northumberland Basin and in the Southern  
315 Uplands.

## 316 5.4 Predicted heat flow

317 We solve the heat flow equation (Eq. 1), using the modelled temperature difference ( $\nabla T$ )  
318 and vertical thermal conductivity ( $k$ ) (e.g. Fig. 7) between temperature nodes at surface and 500 m  
319 below surface, to determine surface heat flow density (Fig. 10). Because the heat flow equation  
320 integrates thermal conductivity and temperature gradient, areas where predicted heat flow is  
321 comparatively elevated with respect to the remainder of our study area do not perfectly conform to  
322 subsurface temperature 'hot spots' (Fig. 8). Instead, areas with elevated surface heat flow density  
323 correspond to regions where shallow subsurface temperatures and bedrock conductivity are high,  
324 such as on the central and eastern parts of the Alston Block and the Lake District. In these areas,  
325 predicted surface heat flow exceeds 90 mW m<sup>-2</sup>. Predicted heat flow in our case study area is more  
326 strictly aligned to depositional settings during early Carboniferous rifting (e.g. Howell *et al.*, 2019)  
327 than subsurface temperature. Comparatively uplifted pre-Carboniferous basement blocks have  
328 overall greater heat flow whereas deeper basins, which were typically infilled by thermally insulating  
329 sedimentary rock, have overall lower heat flow.

## 330 6. Model verification

331 To demonstrate the accuracy of our subsurface temperature model, we compare our  
332 predictions against results from previous studies, including resource maps based on contouring  
333 methods (e.g. Fig. 1), and measured equilibrium borehole temperatures from our case study area.  
334 We also consider variations between results from our thermal model and temperature  
335 measurements that may not be resolved by adopting our predictive modelling technique.

### 336 6.1 Comparisons of modelled and measured subsurface temperature data

337 Overall, there is a wide dispersion of temperatures of temperatures at 1 km depth in our  
338 study area (Fig. 11a). Our mean modelled temperature at 1 km depth of 41.36 °C indicates an  
339 average shallow geothermal gradient of 31.36 °C km<sup>-1</sup>, which is slightly greater than the UK average  
340 of 28 °C km<sup>-1</sup>, although our study area is widely considered to be geothermally hotter than much of  
341 the rest of the UK (Busby *et al.*, 2011). There are broad similarities between the distributions of  
342 modelled hot and cold temperature anomalies (Fig. 8) and previously predicted anomalies based on  
343 contouring (Busby *et al.*, 2011) (Fig. 3).

344 Equilibrium borehole temperature measurements effectively remove drilling induced  
345 transient temperature effects (Oxburgh *et al.*, 1972). Analyzing these data, when possible, should be  
346 considered an integral part of verifying predictive temperature models. Our predicted subsurface  
347 temperatures show strong similarities with measured temperatures from the Rookhope Borehole  
348 (Fig. 11d), which are described in detail by Bott *et al.* (1972). In particular, the decreased geothermal  
349 gradient after approximately 450 m depth below surface is well reproduced by our modelling  
350 methodology. This depth corresponds to the top (Caledonian) basement unconformity, which locally  
351 separates overlying and comparatively thermally insulating Carboniferous sediments from the more  
352 conductive and radiogenic North Pennine Batholith.

353 There are stronger dissimilarities between our predicted subsurface temperatures and  
354 measured equilibrium temperatures from the Newcastle Science Central Deep Geothermal Borehole  
355 (Younger *et al.*, 2016) (Fig. 11e). The implementation of our modelling methodology under-predicts  
356 the temperature gradient with respect to measured temperatures in this region. This under-  
357 prediction could perceptibly be attributed to the spatial variability of thermal properties (*cf.* Fuchs *et al.*,  
358 2020), or to the Ninety Fathom and Stublick fault system, which cuts across this region as well as  
359 geothermally hotter regions to the west (Fig. 2a). If these faults behave as non-sealing conduits, they  
360 may facilitate accelerated heat fluxes via fluid convection (*cf.* Calcagno *et al.*, 2014).

361 The greatest disconnect between predicted and measured equilibrium temperature is  
362 associated with the youngest and most scarcely preserved Carboniferous sediments of our study  
363 area that are encountered in the Becklees borehole (*cf.* Jones *et al.*, 2011) (Fig. 11f). Like  
364 temperatures in the Becklees borehole, our predicted geothermal gradient steepens between 500  
365 and 1000 m depth below surface. For predicted subsurface temperatures, this is due to the presence  
366 of thermally insulating Pennine Coal Measures Group stratigraphy within our geological model  
367 between these depths (Chadwick *et al.*, 1995) (Fig. 4). Instead of encountering a thick succession  
368 solely of this insulating rock unit, however, the Becklees borehole encounters approximately 600 m  
369 of sandstone-rich and variably porous sedimentary rock belonging to the Warwickshire Group,  
370 overlaying an approximately 500 m thick succession of the Pennine Coal Measures Group (Jones *et al.*,  
371 2011) (Fig. 12). These overlaying units are likely to be more conductive due to their compositions  
372 (e.g. Rybach, 1981) and may provide high permeability pathways for heat convection (Kaiser *et al.*,  
373 2011; Scheck-Wenderoth *et al.*, 2014). Modelled subsurface temperatures may be over-predicted  
374 with respect to measured temperatures in the Becklees borehole as a result (Fig. 11f). However, as

375 most of the remainder of Carboniferous sediments in northern England are typically tight (e.g.  
376 Younger *et al.*, 2016), we choose to acknowledge these sources of inaccuracy and maintain our  
377 simplistic, yet more robust, modelling approach.

## 378 6.2 Comparisons of modelled and measured heat flow density data

379 Contoured heat flow density maps provide more precise constraints for our temperature  
380 model, given the greater density of heat flow data in our case study area (Fig. 1b). The two bullseyes  
381 over the Lake District and Alston Block, where heat flow is locally greater than  $90 \text{ mW m}^{-2}$ , are  
382 broadly replicated, as are the lower heat flows in the Northumberland-Solway Basin and Stainmore  
383 Trough (Fig. 10). Our temperature simulations offer greater resolution compared with these  
384 contoured resource maps. Figure 11d shows a cross-plot for measured heat flow data and modelled  
385 data taken from equivalent locations. Overall, there is a positive correlation, suggesting that our  
386 modelling technique successfully replicates areas of greater heat flow density. However, the  
387 dispersion of modelled heat flow density data falls short of equivalent measured data (also see Fig.  
388 11b). This is indicated by the shallow cross-plot gradient of 0.2 (Fig. 11b).

389 At these shallow (<500 m) depths, modelled heat flow inaccuracies could perceivably be  
390 attributed to the neglected influences of superficial deposits, given that in northern England, many  
391 heat flow measurements were recorded in the shallowest tens of metres of the subsurface (Burley  
392 *et al.*, 1984), and that superficial cover thicknesses locally exceed 60 m (McMillan, 2011). Whilst  
393 neglecting the influences of superficial cover has not had a noticeably detrimental effect on  
394 subsurface temperature predictions (e.g. Figs. 8, 11d, e and f), their admission appears to have more  
395 negatively impacted the dispersion of surface heat flow density data (Fig. 11c), because these data  
396 are more directly proportional to the thermal conductivity of the shallow subsurface (Eq. 1). In  
397 temperate regions of the world, including northern England, transient temperature effects relating  
398 to palaeoclimate are proven to also have detrimental effects on shallow heat flow density  
399 predictions (e.g. Slagstad *et al.*, 2009; Majorowicz *et al.*, 2012). A steady-state subsurface  
400 temperature model is, by definition, incapable of accounting for these effects; although a simplistic  
401 alteration to the temperature model's top boundary condition following temperature convergence,  
402 and repeated model iterations, would effectively replicate this transient effect. A surface heat flow  
403 over-estimation would be anticipated had the effects of transient climate adjustment had a  
404 detrimental effect on modelled heat flow data (Majorowicz *et al.*, 2012). Nonetheless, a comparison  
405 between modelled and measured heat flow density data suggests no consistent over-estimation (Fig.  
406 11e).

## 407 7. Discussion and conclusions

408 Predictive subsurface temperature and heat flow density maps can be extracted from our  
409 finite difference models (Figs. 8, 9 and 10) that are more resolute and geologically realistic compared  
410 to maps constructed by contouring around sparsely distributed and often unreliable data points (Fig.  
411 1). Due to our averaging technique, the resolution of our geological model is scarcely compromised  
412 to reduce computational intensity. Its main strengths are its robustness, simplicity, and  
413 reproducibility relative to more elaborate finite element techniques (e.g. Cacace and Jacquey, 2017).  
414 Compared to other finite difference techniques (e.g. Fullea *et al.*, 2009; Keller *et al.*, 2020), our  
415 methodology offers more resolute, geologically more realistic, and quicker solutions for regional  
416 scale (>10 km) problems such as subsurface temperature and heat flow density mapping. The main  
417 inaccuracies of our model in northern England relate to geological inputs, such as bedrock and  
418 superficial cover. Fuchs and Balling (2016) and Fuchs *et al.* (2020) discuss the importance of  
419 geological constraints and their regional variability for subsurface temperature models such as

420 these. Other inaccuracies may relate to fluid convection. When deemed necessary and where data  
421 constraints are sufficient, the incorporation of fluid convection through rock units within  
422 temperature calculations may comprise a simple upgrade on these methods. However, to predict  
423 the influences of more complex structures, such as permeable fault zones, on subsurface  
424 temperature, more elaborate methods and finer resolution models may be necessary (*cf.* Calcagno  
425 *et al.*, 2014). The method presented here represents a useful tool for understanding controls on  
426 subsurface temperature distribution and geothermal potential. MATLAB scripts and program files for  
427 our northern England temperature model are included within the supplementary information.

## 428 Acknowledgements

429 This manuscript contains work conducted during a PhD study undertaken as part of the Natural  
430 Environment Research Council (NERC) Centre for Doctoral Training (CDT) in Oil & Gas [grant number:  
431 NEM00578X/1]. It is sponsored by Natural Environment Research Council, the Keele University Acorn  
432 Fund and the National Productivity Investment Fund (NPIF) whose support is gratefully  
433 acknowledged.

434 We would like to thank three anonymous reviewers for their constructive criticism and feedback  
435 that has helped improve the quality of this manuscript.

436 Our 3D geological model was manipulated using Petrel (Schlumberger) software. Our temperature  
437 modelling technique is supported by the MATLAB (Mathworks) numerical computing environment.

## 438 Conflict of interest

439 The authors declare no conflict of interest.

## 440 Computer code availability

441 Name of code: Geothermal-Modelling

442 Developer: Louis Howell (l.p.howell@keele.ac.uk)

443 Year first available: 2020.

444 Hardware required: Our temperature modelling technique is supported by the MATLAB (Mathworks)  
445 numerical computing environment.

446 Program language: MATLAB.

447 Program size: 30 MB (including geological model).

448 Source code: <https://github.com/lphowell/Geothermal-Modelling>

449

## 450 References

- 451 Adams, C., Monaghan, A. and Gluyas, J., 2019. Mining for heat. *Geoscientist*, 29(4), pp.10-15.  
452 <http://nora.nerc.ac.uk/id/eprint/523186/>
- 453 Bayer, U., Scheck, M. and Köhler, M., 1997. Modeling of the 3D thermal field in the northeast  
454 German basin. *Geologische Rundschau*, 86(2), pp.241-251. <https://doi.org/10.1007/s005310050137>
- 455 Bott, M.H.P., Johnson, G.A.L., Mansfield, J. and Wheilden, J., 1972. Terrestrial heat flow in north-east  
456 England. *Geophysical Journal International*, 27(3), pp.277-288. [https://doi.org/10.1111/j.1365-  
457 246X.1972.tb06093.x](https://doi.org/10.1111/j.1365-246X.1972.tb06093.x)
- 458 BP, 2019. BP Energy Outlook 2019 edition. *London, United Kingdom*.
- 459 British Geological Survey, 2008. *Digital Geological Map of Great Britain 1:625 000 scale (DiGMapGB-  
460 625), Bedrock data. Version 5.17*. Keyworth, Nottingham: British Geological Survey. Release date 11-  
461 2-2008.
- 462 Burley, A.J., Edmunds, W.M. and Gale, I.N., 1984. Investigation of the geothermal potential of the  
463 UK: catalogue of geothermal data for the land area of the United Kingdom.  
464 <http://nora.nerc.ac.uk/id/eprint/512272/>
- 465 Busby, J., Lewis, M., Reeves, H. and Lawley, R., 2009. Initial geological considerations before  
466 installing ground source heat pump systems. *Quarterly Journal of Engineering Geology and  
467 Hydrogeology*, 42(3), pp.295-306. <https://doi.org/10.1144/1470-9236/08-092>
- 468 Busby, J., 2010. Geothermal prospects in the United Kingdom. In: *Proceedings World Geothermal  
469 Congress 2010*, Bali, Indonesia, 25-29 April.  
470 <http://nora.nerc.ac.uk/id/eprint/15965/1/GeothermalProspectsUK.pdf>
- 471 Busby, J., Kingdon, A. and Williams, J., 2011. The measured shallow temperature field in  
472 Britain. *Quarterly Journal of Engineering Geology and Hydrogeology*, 44(3), pp.373-387.  
473 <https://doi.org/10.1144/1470-9236/10-049>
- 474 Busby, J., 2014. Geothermal energy in sedimentary basins in the UK. *Hydrogeology journal*, 22(1),  
475 pp.129-141. <https://doi.org/10.1007/s10040-013-1054-4>
- 476 Busby, L.P., 2019. Thermal conductivity and subsurface temperature data pertaining to the Glasgow  
477 Geothermal Energy Research Field Site (GGERFS). *British Geological Survey Open Report*, OR/19/015.  
478 21pp. <http://nora.nerc.ac.uk/id/eprint/523450/1/OR19015.pdf>
- 479 Cacace, M., Kaiser, B.O., Lewerenz, B. and Scheck-Wenderoth, M., 2010. Geothermal energy in  
480 sedimentary basins: What we can learn from regional numerical models. *Geochemistry*, 70, pp.33-  
481 46. <https://doi.org/10.1016/j.chemer.2010.05.017>
- 482 Cacace, M. and Jacquy, A.B., 2017. Flexible parallel implicit modelling of coupled thermal-  
483 hydraulic-mechanical processes in fractured rocks. *Solid Earth*, 8, pp.921-941.  
484 <https://doi.org/10.5194/se-8-921-2017>
- 485 Calcagno, P., Baujard, C., Guillou-Frottier, L., Dagallier, A. and Genter, A., 2014. Estimation of the  
486 deep geothermal potential within the Tertiary Limagne basin (French Massif Central): An integrated  
487 3D geological and thermal approach. *Geothermics*, 51, pp.496-508.  
488 <https://doi.org/10.1016/j.geothermics.2014.02.002>

489 Čermác, V. and Rybach, L., 1982. Thermal properties: Thermal conductivity and specific heat of  
490 minerals and rocks. *Landolt-Börnstein Zahlenwerte und Funktionen aus Naturwissenschaften und*  
491 *Technik, Neue Serie, Physikalische Eigenschaften der Gesteine*, pp.305-343.

492 Chadwick, B.A., Holliday, D.W., Holloway, S., Hulbert, A.G. and Lawrence, D.J.D., 1995. The structure  
493 and evolution of the Northumberland-Solway Basin and adjacent areas. Subsurface memoir of the  
494 British Geological Survey. London: HMSO.

495 Croucher, A., O'Sullivan, M., O'Sullivan, J., Yeh, A., Burnell, J. and Kissling, W., 2020. Waiwera: A  
496 parallel open-source geothermal flow simulator. *Computers & Geosciences*, p.104529.  
497 <https://doi.org/10.1016/j.cageo.2020.104529>

498 Downing, R.A. and Gray, D.A., 1986a. Geothermal resources of the United Kingdom. *Journal of the*  
499 *Geological Society*, 143(3), pp.499-507. <https://doi.org/10.1144/gsjgs.143.3.0499>

500 Downing, R.A. and Gray, D.A., (eds.) 1986b. Geothermal Energy—the Potential in the United  
501 Kingdom. HMSO, London

502 Fuchs, S. and Balling, N., 2016. Improving the temperature predictions of subsurface thermal models  
503 by using high-quality input data. Part 1: Uncertainty analysis of the thermal-conductivity  
504 parameterization. *Geothermics*, 64, pp.42-54. <https://doi.org/10.1016/j.geothermics.2016.04.010>

505 Fuchs, S., Balling, N. and Mathiesen, A., 2020. Deep basin temperature and heat-flow field in  
506 Denmark—New insights from borehole analysis and 3D geothermal modelling. *Geothermics*, 83,  
507 p.101722. <https://doi.org/10.1016/j.geothermics.2019.101722>

508 Fulla, J., Afonso, J.C., Connolly, J.A.D., Fernandez, M., García-Castellanos, D. and Zeyen, H., 2009.  
509 LitMod3D: An interactive 3-D software to model the thermal, compositional, density, seismological,  
510 and rheological structure of the lithosphere and sublithospheric upper mantle. *Geochemistry,*  
511 *Geophysics, Geosystems*, 10(8). <https://doi.org/10.1029/2009GC002391>

512 Gibson, H., Stüwe, K., Seikel, R., FitzGerald, D., Calcagno, P., Guillen, A., and McInerney, P., 2008.  
513 Forward prediction temperature distribution direct from 3D geology models. In: *Proceedings of the*  
514 *Australian Geothermal Energy Conference*, Melbourne 2008.

515 Hantschel, T. and Kauerauf, A.I., 2009. Introduction to Basin modeling. In: *Fundamentals of Basin*  
516 *and Petroleum Systems Modeling* (pp. 1-30). Springer, Berlin, Heidelberg.

517 Hirst C.M., 2012. The geothermal potential of low enthalpy deep sedimentary basins in the UK. PhD  
518 Thesis, Durham University, UK.

519 Howell, L., Egan, S., Leslie, G. and Clarke, S., 2019. Structural and geodynamic modelling of the  
520 influence of granite bodies during lithospheric extension: application to the Carboniferous basins of  
521 northern England. *Tectonophysics*, 755, pp.47-63. <https://doi.org/10.1016/j.tecto.2019.02.008>

522 Howell, L.P., Besly, B.M., Sooriyathanan, S., Egan, S.S. and Leslie, A.G., *in press*. Seismic and borehole-  
523 based mapping of the late Carboniferous succession in the Canonbie Coalfield, SW Scotland:  
524 evidence for a 'broken' Variscan foreland? *Scottish Journal of Geology*.

525 Jones, N.S., Holliday, D.W. and McKervey, J.A., 2011. Warwickshire Group (Pennsylvanian) red-beds  
526 of the Canonbie Coalfield, England–Scotland border, and their regional palaeogeographical  
527 implications. *Geological Magazine*, 148(1), pp.50-77. <https://doi.org/10.1017/S001675681000035X>

528 Kaiser, B.O., Cacace, M., Scheck-Wenderoth, M. and Lewerenz, B., 2011. Characterization of main  
529 heat transport processes in the Northeast German Basin: Constraints from 3-D numerical  
530 models. *Geochemistry, Geophysics, Geosystems*, 12(7). <https://doi.org/10.1029/2011GC003535>

531 Kimbell, G.S., Young, B., Millward, D. and Crowley, Q.G., 2010. The North Pennine batholith  
532 (Weardale Granite) of northern England: new data on its age and form. *Proceedings of the Yorkshire  
533 Geological Society*, 58(2), pp.107-128. <https://doi.org/10.1144/pygs.58.1.273>

534 Kimbell, G.S., Williamson, J.P., 2015. A gravity interpretation of the Central North Sea. *British  
535 Geological Survey Commissioned Report*, CR/15/119. 75pp.  
536 <http://nora.nerc.ac.uk/id/eprint/516759/1/CR15119.pdf>

537 Lee, M.K., Brown, G.C., Webb, P.C., Wheildon, J. and Rollin, K.E., 1987. Heat flow, heat production  
538 and thermo-tectonic setting in mainland UK. *Journal of the Geological Society*, 144(1), pp.35-42.  
539 <https://doi.org/10.1144/gsjgs.144.1.0035>

540 Majorowicz, J., Gosnold, W., Gray, A., Safanda, J., Klenner, R. and Unsworth, M., 2012. Implications  
541 of post-glacial warming for northern Alberta heat flow-correcting for the underestimate of the  
542 geothermal potential. *GRC Transactions*, 36(GRC1030303).

543 Manning, D.A.C., Younger, P.L., Smith, F.W., Jones, J.M., Dufton, D.J. and Diskin, S., 2007. A deep  
544 geothermal exploration well at Eastgate, Weardale, UK: a novel exploration concept for low-  
545 enthalpy resources. *Journal of the Geological Society*, 164(2), pp.371-382.  
546 <https://doi.org/10.1144/0016-76492006-015>

547 McMillan, A.A., Hamblin, R.J.O., Merritt, J.W., 2011. A lithostratigraphical framework for onshore  
548 Quaternary and Neogene (Tertiary) superficial deposits of Great Britain and the Isle of Man. *British  
549 Geological Survey Research Report*, RR/10/03. 343pp.  
550 <http://nora.nerc.ac.uk/id/eprint/14531/1/RR10003.pdf>

551 Monaghan, A., Starcher, V., Barron, H., Kuras, O., Abesser, C., Midgley, J., Dochartaigh, B.Ó., Fordyce,  
552 F., Burke, S., Taylor-Curran, H. and Luckett, R., 2019. A new Mine Water Geothermal Research  
553 Facility: the UK Geoenergy Observatory in Glasgow, Scotland. In *81st EAGE Conference and  
554 Exhibition 2019* (Vol. 2019, No. 1, pp. 1-5). European Association of Geoscientists & Engineers.  
555 <https://doi.org/10.3997/2214-4609.201901602>

556 Norden, B. and Forster, A., 2006. Thermal conductivity and radiogenic heat production of  
557 sedimentary and magmatic rocks in the Northeast German Basin. *AAPG bulletin*, 90(6), pp.939-962.  
558 <https://doi.org/10.1306/01250605100>

559 Norden, B., Förster, A. and Balling, N., 2008. Heat flow and lithospheric thermal regime in the  
560 Northeast German Basin. *Tectonophysics*, 460(1-4), pp.215-229.  
561 <https://doi.org/10.1016/j.tecto.2008.08.022>

562 Norden, B., Förster, A., Förster, H.J. and Fuchs, S., 2020. Temperature and pressure corrections  
563 applied to rock thermal conductivity: impact on subsurface temperature prognosis and heat-flow  
564 determination in geothermal exploration. *Geothermal Energy*, 8(1), pp.1-19.  
565 <https://doi.org/10.1186/s40517-020-0157-0>

566 Oxburgh, E.R., Richardson, S.W., Turcotte, D.L. and Hsui, A., 1972. Equilibrium bore hole  
567 temperatures from observation of thermal transients during drilling. *Earth and Planetary Science  
568 Letters*, 14(1), pp.47-49. [https://doi.org/10.1016/0012-821X\(72\)90077-5](https://doi.org/10.1016/0012-821X(72)90077-5)

569 Paulillo, A., Cotton, L., Law, R., Striolo, A. and Lettieri, P., 2020. Geothermal energy in the UK: the  
570 life-cycle environmental impacts of electricity production from the United Downs Deep Geothermal  
571 Power project. *Journal of Cleaner Production*, 249, p.119410.  
572 <https://doi.org/10.1016/j.jclepro.2019.119410>

573 Pérez-Zárate, D., Santoyo, E., Acevedo-Anicasio, A., Díaz-González, L. and García-López, C., 2019.  
574 Evaluation of artificial neural networks for the prediction of deep reservoir temperatures using the  
575 gas-phase composition of geothermal fluids. *Computers & Geosciences*, 129, pp.49-68.  
576 <https://doi.org/10.1016/j.cageo.2019.05.004>

577 Rollin, K.E., 1995. A simple heat-flow quality function and appraisal of heat-flow measurements and  
578 heat-flow estimates from the UK Geothermal Catalogue. *Tectonophysics*, 244(1-3), pp.185-196.  
579 [https://doi.org/10.1016/0040-1951\(94\)00227-Z](https://doi.org/10.1016/0040-1951(94)00227-Z)

580 Rybach, L. 1981. Geothermal systems, conductive heat flow, geothermal anomalies. *In*: Rybach, L.  
581 and Muffler, L.J.P. (eds.), *Geothermal Systems: Principles and Case Histories*. Wiley, Chichester, 3-36.

582 Scheck-Wenderoth, M., Cacace, M., Maystrenko, Y.P., Cherubini, Y., Noack, V., Kaiser, B.O., Sippel, J.  
583 and Björn, L., 2014. Models of heat transport in the Central European Basin System: Effective  
584 mechanisms at different scales. *Marine and Petroleum Geology*, 55, pp.315-331.  
585 <https://doi.org/10.1016/j.marpetgeo.2014.03.009>

586 Sclater, J.G. and Christie, P.A., 1980. Continental stretching: An explanation of the post-mid-  
587 Cretaceous subsidence of the central North Sea basin. *Journal of Geophysical Research: Solid*  
588 *Earth*, 85(B7), pp.3711-3739. <https://doi.org/10.1029/JB085iB07p03711>

589 Slagstad, T., Balling, N., Elvebakk, H., Midttømme, K., Olesen, O., Olsen, L. and Pascal, C., 2009. Heat-  
590 flow measurements in Late Palaeoproterozoic to Permian geological provinces in south and central  
591 Norway and a new heat-flow map of Fennoscandia and the Norwegian–Greenland  
592 Sea. *Tectonophysics*, 473(3-4), pp.341-361. <https://doi.org/10.1016/j.tecto.2009.03.007>

593 Terrington, R.L. and Thorpe, S., 2014. Metadata report for the Northumberland and Solway Basin  
594 1:250 000 geological model. British Geological Survey Open Report, OR/13/049. 20pp.  
595 <http://nora.nerc.ac.uk/id/eprint/507069/1/OR13049.pdf>

596 Vilà, M., Fernández, M. and Jiménez-Munt, I., 2010. Radiogenic heat production variability of some  
597 common lithological groups and its significance to lithospheric thermal modeling. *Tectonophysics*,  
598 490(3-4), pp.152-164. <https://doi.org/10.1016/j.tecto.2010.05.003>

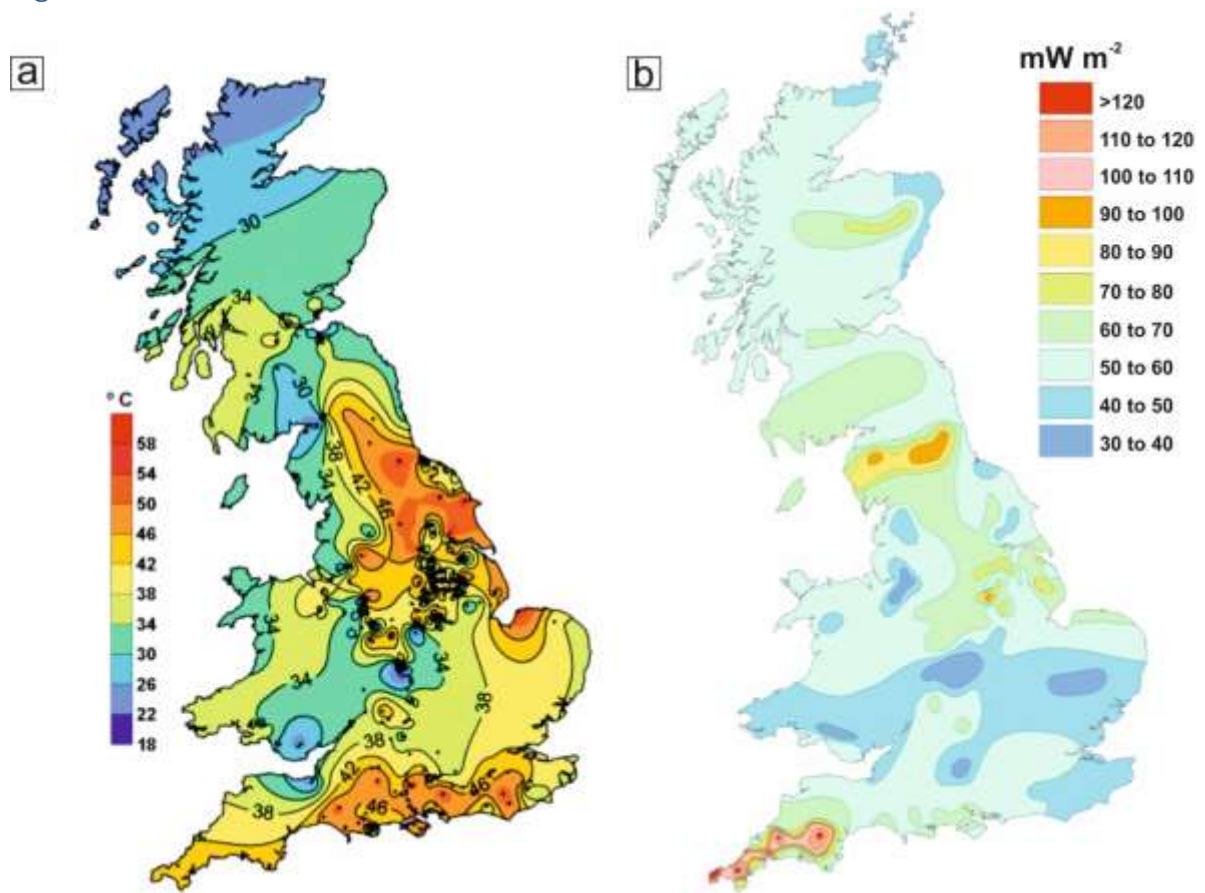
599 Younger, P.L., Manning, D.A., Millward, D., Busby, J.P., Jones, C.R. and Gluyas, J.G., 2016. Geothermal  
600 exploration in the Fell Sandstone Formation (Mississippian) beneath the city centre of Newcastle  
601 upon Tyne, UK: the Newcastle Science Central deep geothermal borehole. *Quarterly Journal of*  
602 *Engineering Geology and Hydrogeology*, 49(4), pp.350-363. <https://doi.org/10.1144/qjegh2016-053>

603 Zhang, X., Lyu, D., Li, P., Jin, X., Liaw, P.K. and Keer, L.M., 2019. A closed-form solution for the  
604 horizontally aligned thermal-porous spheroidal inclusion in a half-space and its applications in  
605 geothermal reservoirs. *Computers & Geosciences*, 122, pp.15-24.  
606 <https://doi.org/10.1016/j.cageo.2018.10.001>

607

608 Figures

609 Figure 1

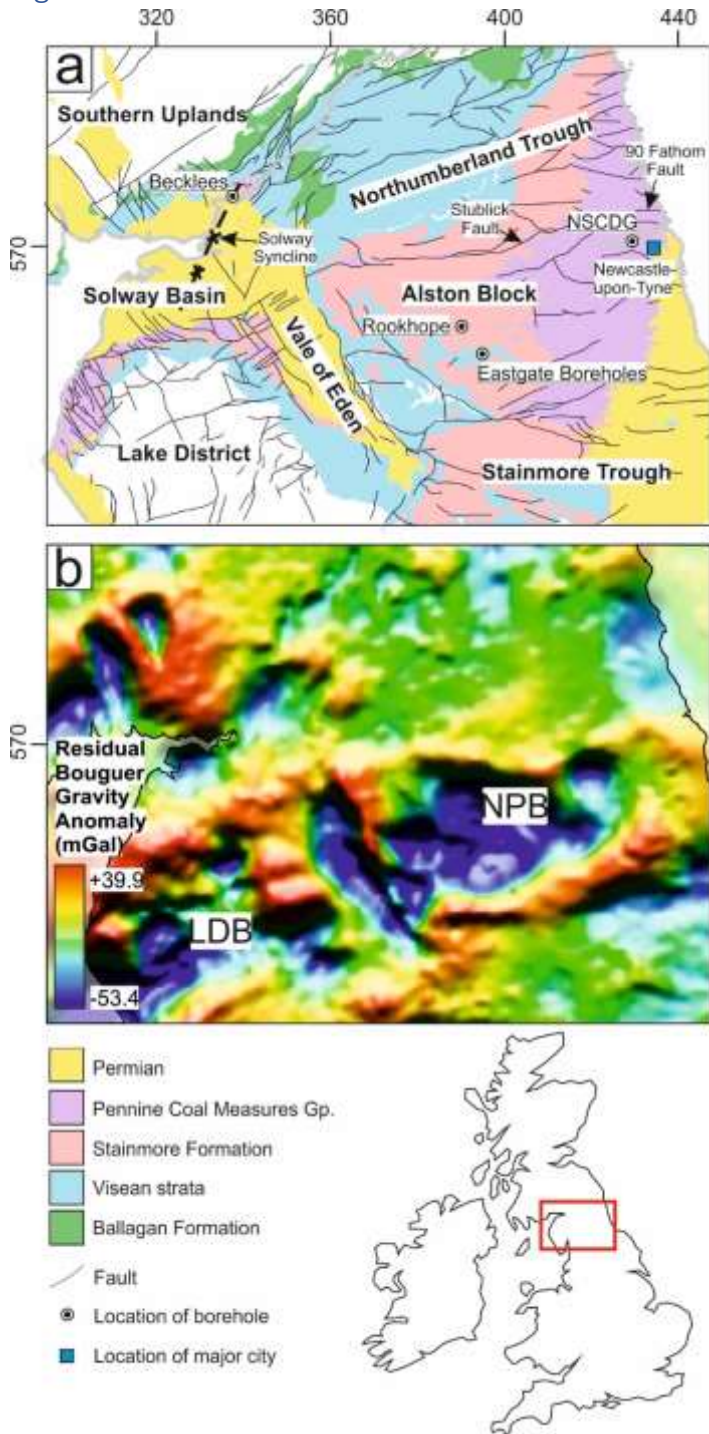


610

611 Fig. 1a: UK subsurface temperature maps for 1 km depth (from Busby *et al.*, 2011). 1b: UK heat flow  
612 maps (from Downing and Gray, 1986).

613

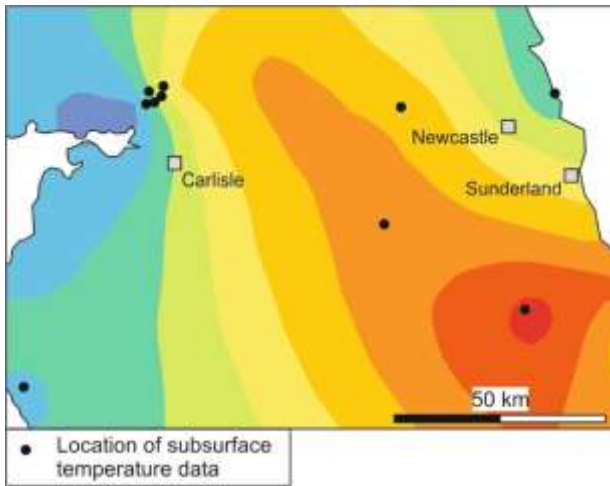
614 Figure 2



615

616 Fig. 2a: A geological map for our case study area (British Geological Survey, 2008) with annotated  
617 structural features and borehole locations. 2b: A Bouguer gravity anomaly survey for our case study  
618 area (Kimbell and Williamson, 2015) with annotations for the negative gravitational anomalies  
619 associated with the Lake District Batholith (LDB) and the North Pennine Batholith (NPB). British  
620 National Grid coordinates are used for these and all maps in this manuscript. Both figures 2a and 2b  
621 show the same area of the UK.

622 Figure 3

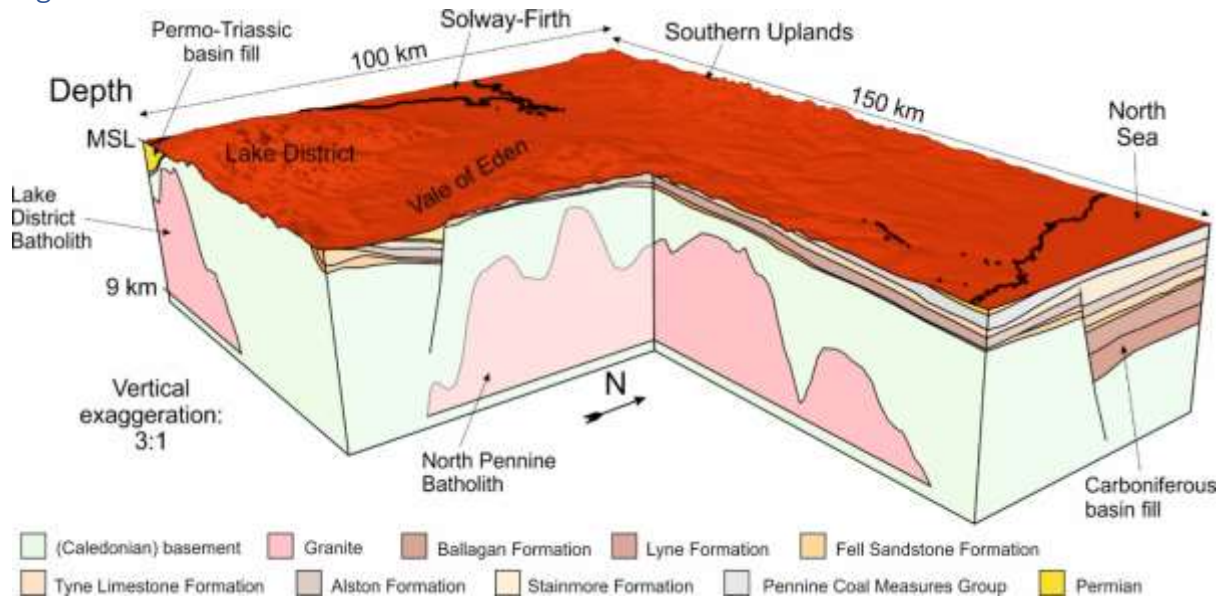


623

624 Fig. 3: Subsurface temperature contours (from Fig. 1a) and locations of data points (*cf.* Burley *et al.*,  
625 1984).

626

627 Figure 4

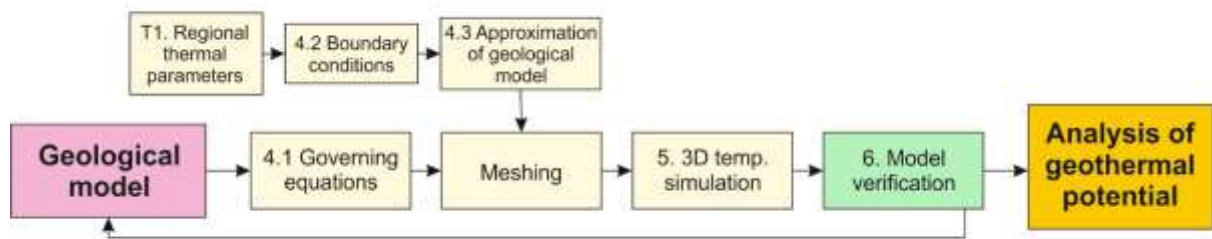


628

629 Fig. 4: A schematic illustration of our 3D geological model. Carboniferous basin structure after  
630 Chadwick *et al.* (1995) and Caledonian granite thicknesses after Kimbell *et al.* (2010). As with Kimbell  
631 *et al.* (2010), our model assumes flat bases to the batholiths at 9 km depth. This is a simplification of  
632 uncertain geology. MSL = mean sea level. The depicted 3D model was produced using Petrel  
633 (Schlumberger) software.

634

635 Figure 5

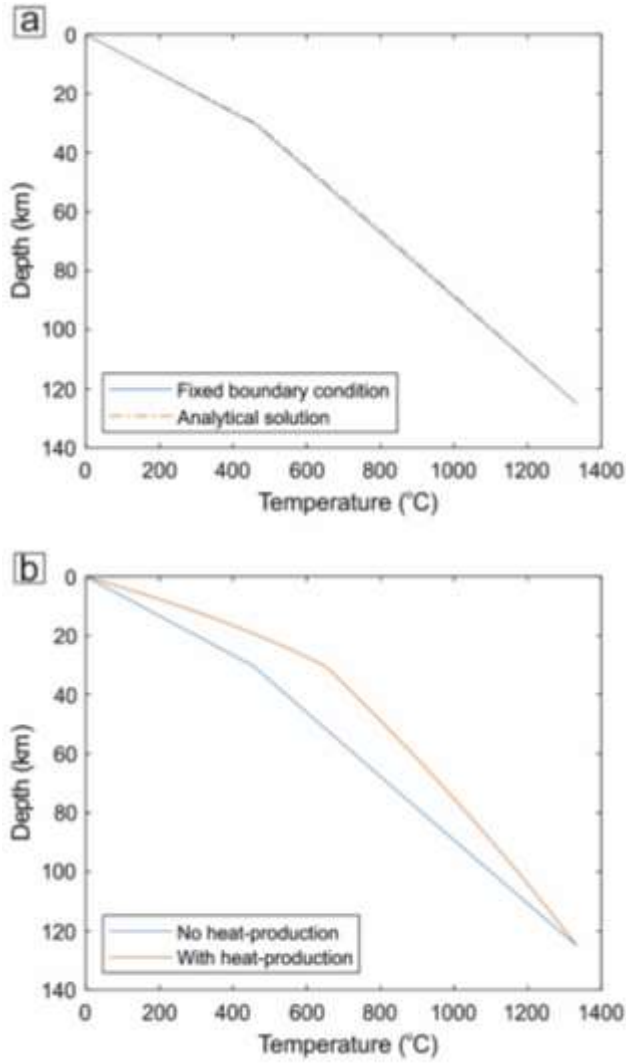


636

637 Fig. 5: An illustrated summary of our modelling approach. Numbering of method steps correspond to  
638 sections or tables within this manuscript, in which these steps are described.

639

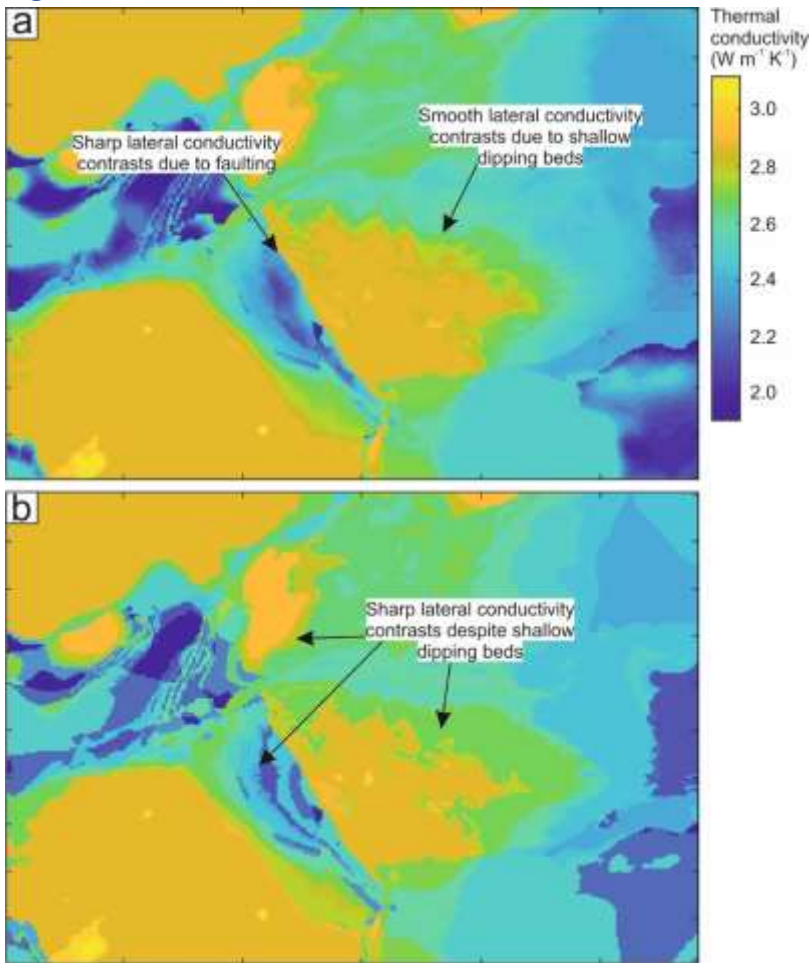
640 Figure 6



641

642 Fig. 6a: A comparison between analytical and fixed boundary condition solutions for one-  
643 dimensional lithosphere-scale non-homogeneous conductive heat flow. See Table 1 for modelling  
644 parameters. 6b: A comparison between fixed boundary condition solutions for one-dimensional  
645 lithosphere-scale non-homogeneous conductive heat flow with no internal heat production ( $Q$ ) and  
646 with internal heat production.

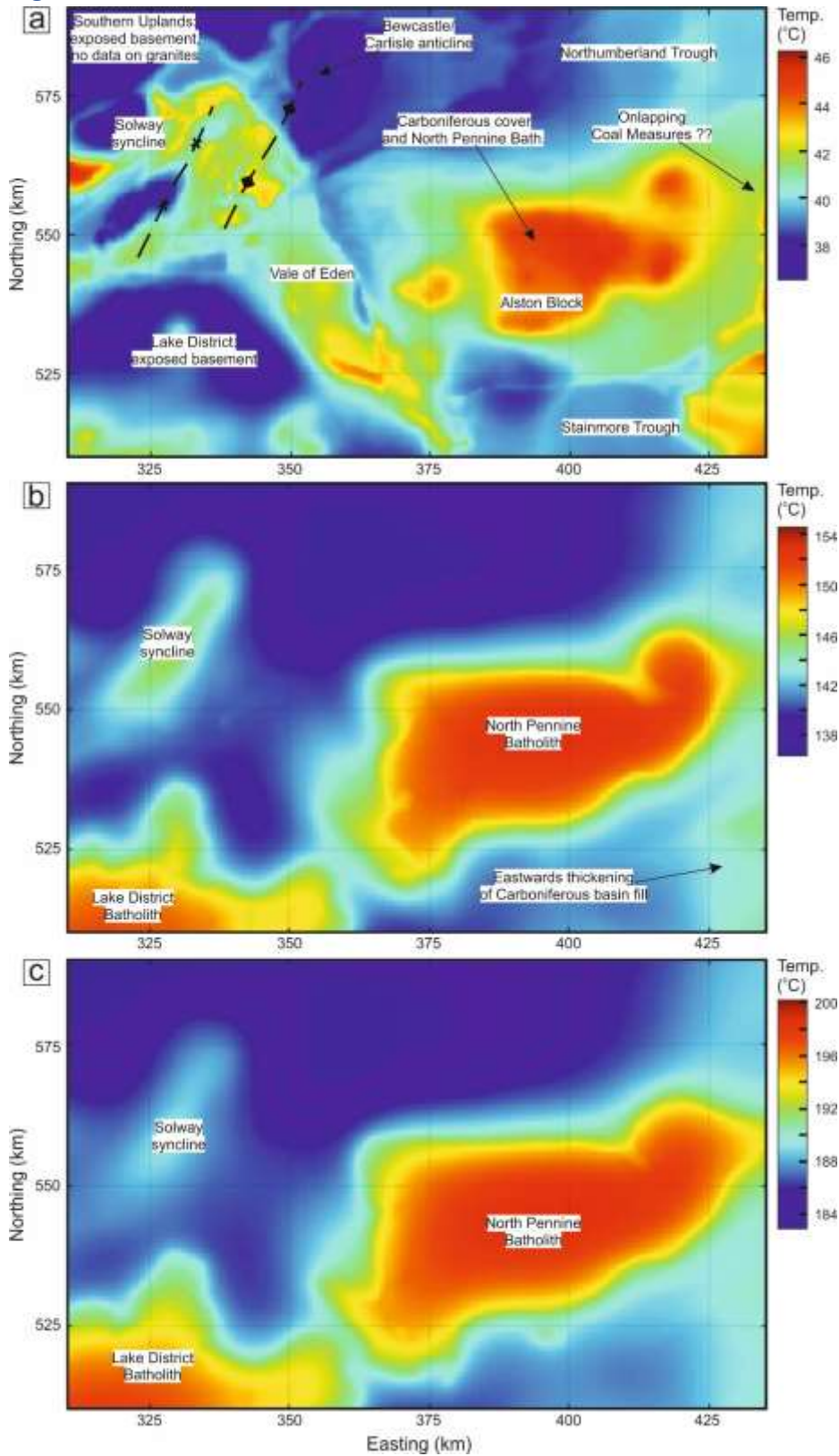
647 Figure 7



648

649 Fig. 7a: Vertical thermal conductivity tensors between 500 m and 1000 m below surface determined  
650 by calculating the harmonic mean of multiple values between these two depths for northern  
651 England. 7b: Vertical thermal conductivity tensors between 500 m and 1000 m below surface  
652 determined by calculating the harmonic mean of just the two values at temperature nodes. For  
653 thermal conductivity values of rock units see Table 1.

654

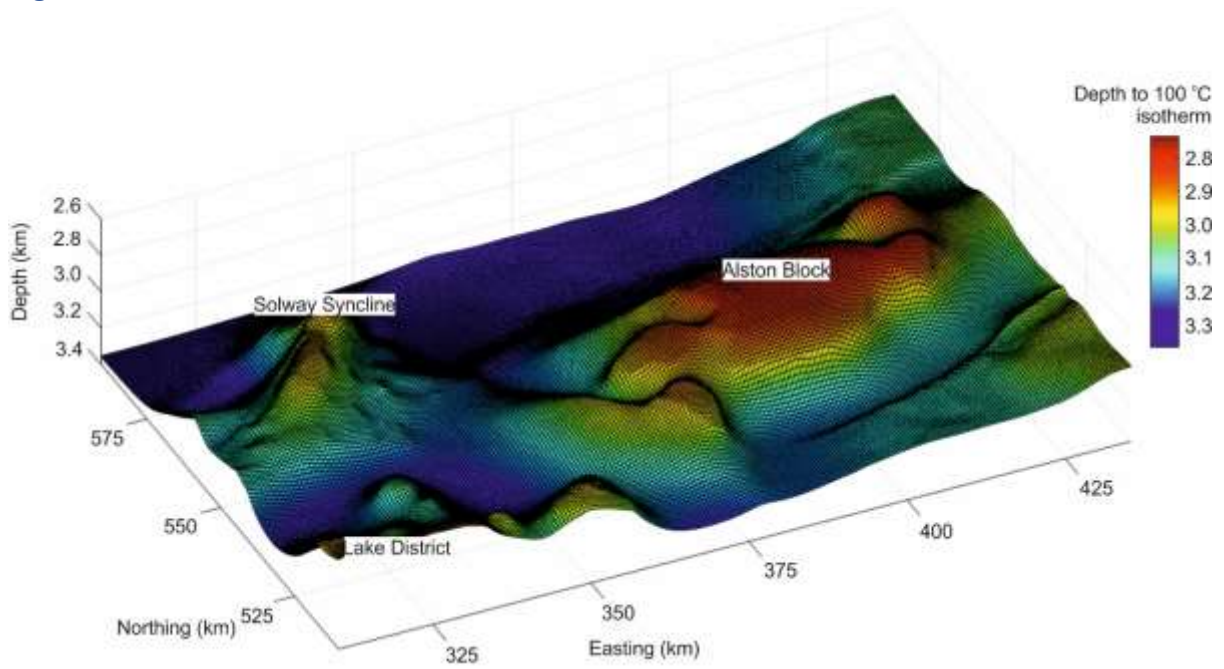


656

657 Fig. 8a: Modelled temperature at 1 km depth. Compare with Fig. 1b (Busby *et al.*, 2011). 8b:

658 Modelled temperature at 5 km depth. 8c: Modelled temperature at 7 km depth.

659 Figure 9

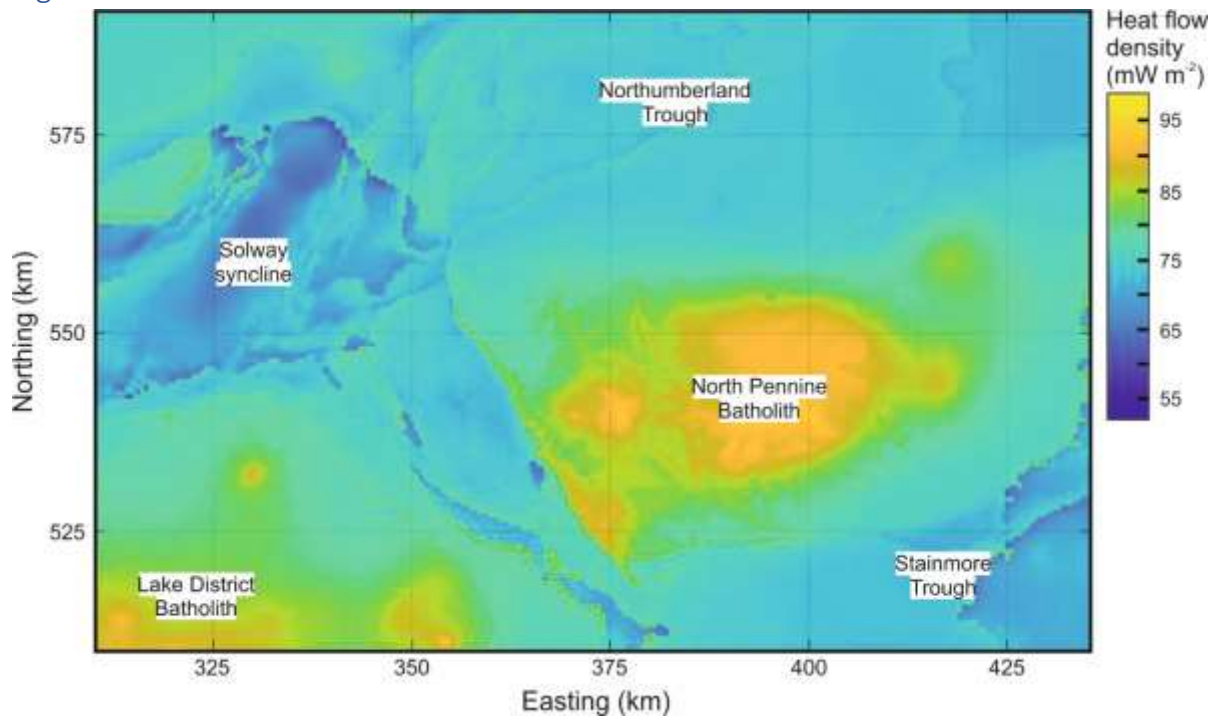


660

661 Fig. 9: Modelled depth to the 100 °C isotherm.

662

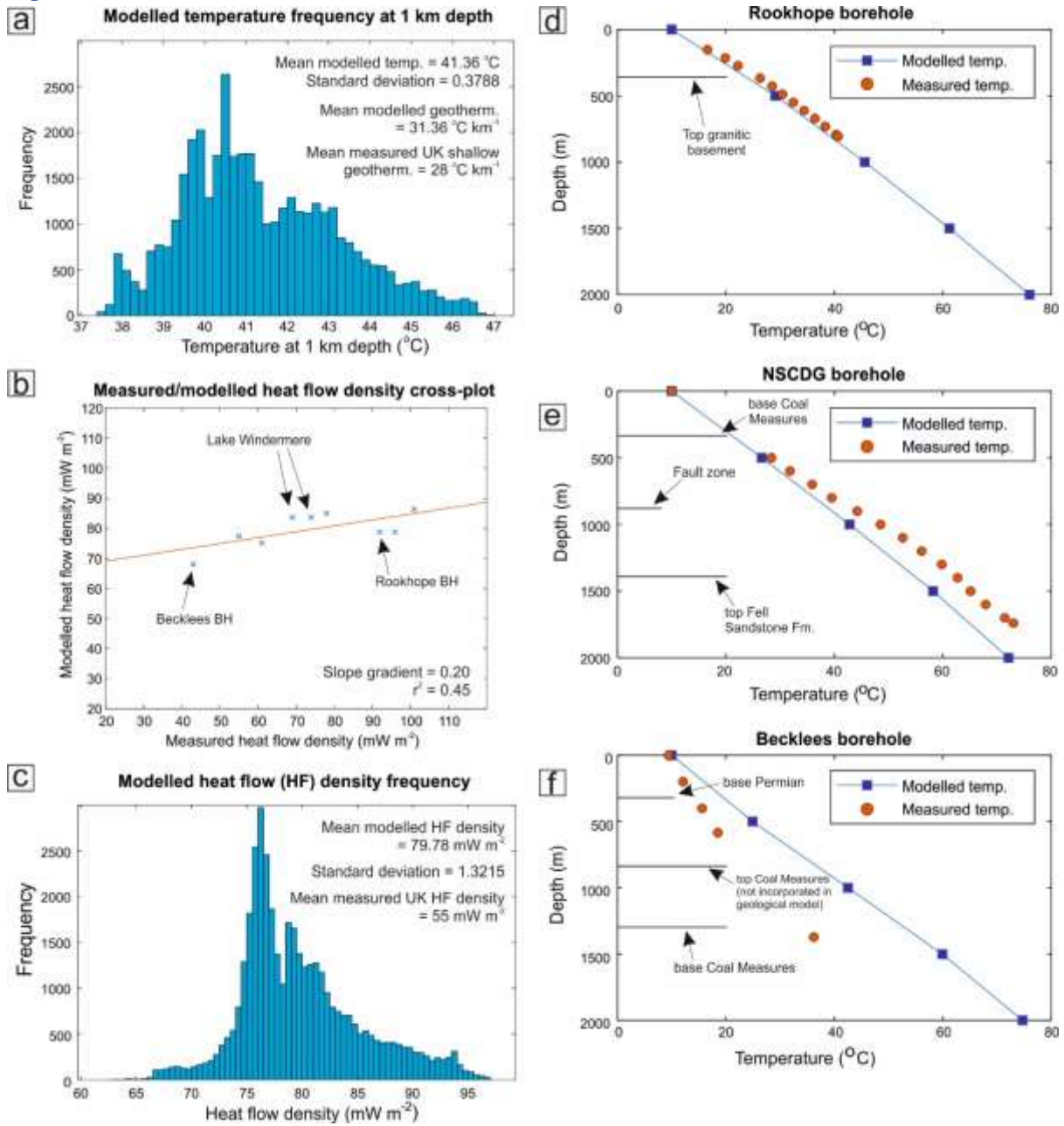
663 Figure 10



664

665 Fig. 10: Modelled surface (500 m below surface to surface) heat flow density map for northern  
666 England based on predicted subsurface temperatures and vertical conductivity values. Compare with  
667 Fig. 1b (Downing and Gray, 1986a).

668

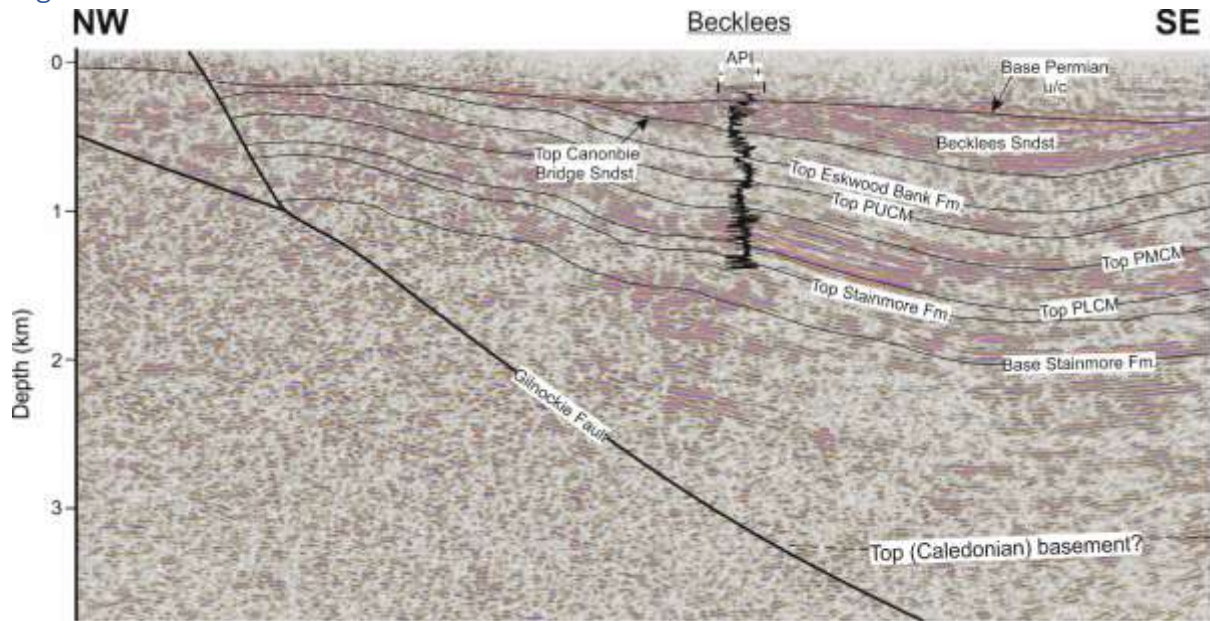


670

671 Fig. 11a: A cross-plot between measured heat flow density data and modelled data in our study  
 672 area. Modelled data are taken from approximately the equivalent location as measured data. 11b  
 673 and c: Frequency charts for modelled temperature values at 1 km depth, and shallow (<500 m)  
 674 heat flow density values, respectively. Mean measured UK shallow (<1 km) geothermal gradient and  
 675 mean measured UK heat flow density taken from Busby *et al.* (2011) and Busby (2010). 11d, e and f:  
 676 Comparisons between modelled subsurface temperatures and measured equilibrium borehole  
 677 temperatures for the Rookhope Borehole, the Newcastle Science Central Deep Geothermal Borehole  
 678 and the Becklees Borehole, respectively. For locations of boreholes, see Figure 3a. Measured  
 679 equilibrium boreholes temperatures taken from Burley *et al.* (1984) and Younger *et al.* (2016).

680

681 Figure 12



682

683 Fig. 12: A seismic reflection profile intersecting the Becklees borehole. A vertical gamma ray profile  
684 for the Becklees borehole is illustrated. The Warwickshire Group comprises the Eskbank Wood,  
685 Canonbie Bridge Sandstone and Becklees Sandstone formations (*cf. Jones et al., 2011*). The Pennine  
686 Coal Measures Group comprises the Pennine Lower Coal Measures (PLCM), Pennine Middle Coal  
687 Measures (PMCM) and Pennine Upper Coal Measures (PUCM) formations. Seismic interpretation  
688 based on Howell *et al.* (in press). Seismic courtesy of the UK Onshore Geophysical Library (UKOGL).

689

## 690 Tables

Geological unit	Thermal conductivity ( $\text{W m}^{-1} \text{K}^{-1}$ )	RHP ( $\mu\text{W m}^{-3}$ )	Reference
Lower Permian	2.5	1.0	Norden and Förster (2006)
Pennine Coal Measures Group	1.9	0.92	Downing and Gray (1986)
Stainmore Formation	2.38	0.88	Younger <i>et al.</i> (2016)
Alston Formation	2.5	0.88	Younger <i>et al.</i> (2016)
Tyne Limestone Formation	2.7	0.85	Younger <i>et al.</i> (2016)
Fell Sandstone Formation	2.6	0.85	Younger <i>et al.</i> (2016)
Lyne Formation	2.7	0.85	Younger <i>et al.</i> (2016)
Ballagan Formation	2.92	0.85	Downing and Gray (1986b)
Pre-Carboniferous (Caledonian) basement	2.87	1.49	Downing and Gray (1986b)
Granite Batholiths	3.1	4.1	Downing and Gray (1986b); Manning <i>et al.</i> (2007)
Middle-Lower crust	3.1-2.2	1.5	Norden <i>et al.</i> (2008); Vila <i>et al.</i> (2010)
Mantle	4.1	0.1	Vila <i>et al.</i> (2010)

691 Table 1: Regional thermal parameters for temperature simulation.

692

693 Supplementary information

694 MATLAB project files ([https://github.com/lphowell/Geothermal-](https://github.com/lphowell/Geothermal-Modelling/tree/master/Geothermal_NEngland)  
695 [Modelling/tree/master/Geothermal\\_NEngland](https://github.com/lphowell/Geothermal-Modelling/tree/master/Geothermal_NEngland)).

696